RSC Advances

PAPER

View Article Online
View Journal | View Issue

Cite this: *RSC Adv.*, 2020, **10**, 43233

Cell-tailored calcium carbonate particles with different crystal forms from nanoparticle to nano/microsphere†

Yi Chang,[a] Huijuan Han,[b] Tingting Liu,[a] Shibao Yuan,[c] Shuting Chen,[a] Yuming Guo, *[c] Lin Yang [a] and Xiaoming Ma *[a]

Inspired by biomineralization, the first synthesis of size-tunable calcium carbonates from nanoparticles (YC-$CaCO_3$ NPs) to nano/microspheres (YC-$CaCO_3$ N/MSs) with a porous structure was accomplished using a facile method under the mediation of the secretion from yeast cells (YCs). The biomolecules derived from the secretion of YCs were used as conditioning and stabilizing agents to control the biosynthesis of the YC-$CaCO_3$ materials. The morphology and crystal forms of YC-$CaCO_3$ materials can be affected by the biomolecules from the secretion of YCs. With increasing concentrations of biomolecules, the morphologies of the obtained $CaCO_3$ materials changed from nanoparticles to nano/microspheres with a porous structure, while the crystal forms transformed from amorphous to calcite. Functional investigations showed that YC-$CaCO_3$ NSs with a porous structure effectively acted as anticancer drug carriers with accurate and selective drug release in tumor tissue, which suggests that they have great potential to function as a therapeutic delivery system. These application features are mainly attributed to the satisfactory biocompatibility and biodegradability, high drug-loading capacity, and pH-dependent sustained drug release performance of the porous YC-$CaCO_3$ NSs. The biomimetic synthesis strategy of YC-$CaCO_3$ materials mediated by YC secretion not only helps to shed light on the biomineralization mechanism in organisms, but may also lead to a new means of biosynthesizing organic–inorganic nanocomposites.

Received 28th August 2020
Accepted 6th November 2020

DOI: 10.1039/d0ra07393h

rsc.li/rsc-advances

1. Introduction

Research on biomineralization requires that the fields of biology and chemistry become relatively interdependent.[1–3] Natural organisms, both simple single-celled organisms and the higher organisms, with abundant organics and a highly organized extra- and intracellular microenvironment, can precisely induce and regulate the biosynthesis of inorganic–organic hybrid nano/micromaterials with finely tuned sizes and morphologies.[4,5] For example, magnetosome nanocrystals (Fe_3O_4 or Fe_3S_4) with a chain arrangement can be intracellularly biosynthesized under the mediation of proteins from magnetotactic bacteria.[6,7] Silica with hierarchical structures can be established and patterned on a DNA origami template under the control of silicatein and silaffins found in diatoms and sponges.[8–10] Sulfur bacteria can induce and oxidize natural reductive sulfides into sulfur or sulfuric acid under the direction of the intracellular proteins.[11] Thus, the construction of nanomaterials utilizing the potential of microorganisms can open a new avenue for "green" synthesis.[12,13]

During the organism-mediating biomineralization process, organic matrixes are used to guide the orientation of enrichment on the surface network of nano/micromaterials according to organic–inorganic interface molecular recognition, which plays a key role in the formation of different morphologies and crystallographic orientation when materials grow from the nanometer scale to the macroscopic scale.[14–18] Furthermore, the organic–inorganic hybrid materials that result contain inorganic phase nano/micromaterials and a certain amount of organic matrix, with good biocompatibility and extraordinary mechanical strength and toughness properties, and they also exhibit some novel performances different from their natural functions observed in the fields of biology, pharmacology, and environmentology.[18–21] Thus, the biomimetic approach based on mimicry of the natural biofabrication process might provide a versatile and effective alternative for the green synthesis of functional nanomaterials.[22–24]

Calcium carbonate, which is one of the most common biominerals, exhibits various morphologies and crystal forms in

[a]Key Laboratory of Green Chemical Media and Reactions, Ministry of Education, Henan Normal University, Xinxiang, Henan, 453007, P. R. China. E-mail: mxm@htu.edu.cn

[b]School of Chemistry and Chemical Engineering, Henan Institute of Science and Technology, Xinxiang, Henan 453007, P. R. China

[c]Collaborative Innovation Center of Henan Province for Green Manufacturing of Fine Chemicals, School of Chemistry and Chemical Engineering, Henan Normal University, Xinxiang, Henan, 453007, P. R. China

† Electronic supplementary information (ESI) available. See DOI: 10.1039/d0ra07393h

biological systems, which results in different functions. For example, hierarchical $CaCO_3$ micromaterials with vaterite and aragonite types exist in otolith work as balancers and gravitational receptors in organisms.[25] Multilayer $CaCO_3$ in four forms (calcite, aragonite, vaterite, or amorphous) is present in the skeletons of mollusks and seashells to support and protect the organisms.[26] Calcium carbonate in biological systems is multifunctional because it combines inorganic phase $CaCO_3$ with a certain amount of organic matter.

Based on their predominant properties, there has been wide interest and active research in the construction of different morphologies of $CaCO_3$ nanomaterials with varied structures in biological systems.[26,27] In previous reports, we introduced some intra- and extracellular $CaCO_3$ nano/micromaterials with different morphologies and complex structures, and further explored their potential applications in carrying anticancer drugs and removing heavy metal ions from water.[28–32] We found that each unique reactive environment is significantly associated with the structures, shapes, and sizes of $CaCO_3$ nano/micromaterials, which results in different specific surface areas and pore sizes, and the environment will further affect their performances in different fields.[33–35]

Herein, inspired by the biomineralization of natural $CaCO_3$, we report the biomimetic synthesis of $CaCO_3$ based on biological concepts and mechanisms, and mediated by yeast cell secretion. The biomolecules derived from the secretion of yeast cells were used as conditioning and stabilizing agents to control the biosynthesis of the yeast cell (YC)-$CaCO_3$ materials. The concentrations of reactants were systematically investigated to achieve a controllable and reliable design of $CaCO_3$ with different morphologies and sizes. It was demonstrated that the particle crystallinity (from the amorphous state to calcite phase) depends on the concentrations of reactants and the reaction time. With the increase in the concentrations of biomolecules, the morphologies and crystal forms of the $CaCO_3$ materials obtained changed from nanoparticles to nano/microspheres and from amorphous to calcite, respectively. Furthermore, we used YC-$CaCO_3$ nanospheres (NSs) as an anticancer drug carrier for doxorubicin hydrochloride (DOX), a clinically used antitumor drug, and showed that they can selectively and effectively release the drug in the tumor tissue, suggesting their potential application in promising therapeutics.[31,36]

2. Experimental section

2.1 Materials

Instant dry yeast was purchased from Angel Yeast Co., Ltd. and peptone and glucose ($C_6H_{12}O_6$) were purchased from Beijing Aobox Biotechnology Co., Ltd. Calcium chloride ($CaCl_2$) and sodium carbonate (Na_2CO_3) were used as received without further purification. Doxorubicin hydrochloride (DOX-HCl, Beijing Huafeng United Technology Co., Ltd., China) was used as a model drug to examine the pH-responsive anticancer drug carrier. Water was deionized through a Nex Power 1000 water purification system (Human Corporation). Dulbecco's modified Eagle's medium (DMEM) with penicillin and streptomycin, fetal bovine serum (FBS), and 3-(4,5-dimethylthia-zol-2-yl)-2,5-diphenyltetrazolium bromide (MTT) were purchased from Beijing Solarbio Science & Technology Co., Ltd. In addition, other reagents were of analytical grade and purchased from Sinopharm Group Co., Ltd. (Shanghai, China). All chemicals were used as received without further purification.

2.2 Characterizations

The structure and phase composition of $CaCO_3$ NSs were characterized by X-ray powder diffraction (XRD) measurements on a BrukerD and Advance X-ray powder diffractometer with graphite monochromatized Cu Kα ($l = 0.15406$ nm). A scanning rate of $0.05^\circ\ s^{-1}$ was applied to record the pattern in the 2θ range of 10–80°. The Fourier transform infrared (FT-IR) spectra were recorded on a Bio-Rad FTS-40 Fourier transform infrared spectrometer in the wavenumber range of 4000–400 cm^{-1}. The spectra were collected at 2 cm^{-1} resolution with 128 scans by preparing KBr pellets with a 3 : 100 sample-to-KBr ratio. Differential thermal analysis-thermogravimetry (DTA-TG) was performed on a ZRY-1P at a heating rate of 10 °C min^{-1} in air flow.

The morphology of the samples was observed using a JSM-6390LV scanning electron microscope and a SUPRA40 field emission scanning electron microscope. Field emission scanning electron microscopy-energy dispersive X-ray spectroscopy (FESEM-EDS) analysis was conducted to observe the elemental distribution. Transmission electron microscopy (TEM) analyses were performed using an FEI Tecnai G2 20 transmission electron microscope equipped with selected area electron diffraction (SAED), and were used to confirm the particle size and determine the nanosphere structures. To prepare for TEM, the samples were first degassed at 300 °C for 4 h before analysis. Then, 5 μL droplets of dilute alcohol solution were dripped onto carbon-coated copper grids. N_2 adsorption–desorption analysis was performed at 77 K using a Micromeritics ASAP 2020 analyzer.

The Brunauer–Emmett–Teller (BET) model was adopted to calculate the specific surface areas, and the pore size distribution was derived from the desorption branch of the isotherms utilizing the Barret–Joyner–Halenda (BJH) model. The total pore volume was estimated from the amounts of N_2 adsorbed at a relative pressure (P/P_0) of 0.99. Fluorescent images were acquired using a TCS NT confocal laser scanning microscope (Leica, Germany). A TU-1900 UV/vis spectrophotometer was used to determine the absorbance of DOX, and also to determine the concentration of the DOX solution.

2.3 Biomimetic synthesis of YC-$CaCO_3$

Yeast cells were grown with aeration at 30 °C in sterilized culture medium. According to a typical procedure, 1 g peptone and 1 g glucose were dissolved in 50 mL of deionized water in a 200 mL Erlenmeyer flask. The Erlenmeyer flask was placed in an autoclave for 20 min at high temperature (110 °C). Then, after the flask cooled to room temperature, 0.33 g yeast cells were added. The yeast cells were cultured with continuous agitation (200 rpm) for 24 h at 30 °C. After the yeast cells exhibited reproduction (Fig. S1†), the yeast solution (20 mL) was

centrifuged at 5000 rpm for 8 min to remove the yeast cells and obtain the secretion from the yeast cells.

Then, $CaCl_2$ (40 mL) solution at various concentrations (from 0.02 to 0.3 M) was added to the upper secretion with continuous stirring (300 rpm, 25 °C) for 12 h. The same concentration of Na_2CO_3 (40 mL) was also added to the above solution with continuous stirring (300 rpm, 25 °C) for 30 min. The $CaCO_3$ nanomaterials produced by mediation with yeast cells (YC-$CaCO_3$) were harvested by centrifuging at 5000 rpm for 5 min, thoroughly rinsed with distilled water and ethanol, washed, and dried in a vacuum drying oven (40 °C) for 24 h.

2.4 Loading of DOX into YC-$CaCO_3$ NSs *in vitro*

Herein, due to the porous structure and the considerable yield, nanospheres 500 nm in diameter were chosen to evaluate their behavior as an anticancer drug carrier. DOX solution was easily loaded into the YC-$CaCO_3$ NSs by co-incubation. For this procedure, 4 mg of the as-prepared YC-$CaCO_3$ NSs was added to 7 mL DOX aqueous solution (10 mg per 100 mL). The mixture was shaken in a thermostatic shaker at 100 rpm for 24 h at 30 °C. Then, the products were collected by centrifugation and washed with double-distilled water until the supernatant was colorless, and free DOX was thoroughly removed by washing. Finally, the products were dried under vacuum at 30 °C for 24 h.

A powder of the YC-$CaCO_3$ NSs loaded with DOX (denoted as YC-$CaCO_3$-DOX) was obtained. The loading capacity was determined by measuring the absorbance of 5 mg of YC-$CaCO_3$-DOX in HCl at 480 nm. The results showed that the weight percentage of DOX in the product was 5.08%, which meets the requirement of the anticancer drug formula in the drug delivery system.[36]

2.5 Release of DOX from YC-$CaCO_3$-DOX *in vitro*

The pH of normal tissues is approximately 7.4, while that of tumor sites is approximately 5.[36–38] Therefore, the release of DOX under different pH conditions adjusted by physiological buffer solutions (PBS) (from 4.0 to 7.4) was determined. Among these different systems, the solutions of pH 7.4 and 4.5 simulated the pH conditions of normal tissue and a tumor site, respectively. To perform these experiments, 6 mg YC-$CaCO_3$-DOX was added to the PBS buffer solutions with different pH values (7 mL), and the suspensions were incubated in a thermostatic shaker (37 °C, 150 rpm) for DOX release.

At predetermined intervals, 3 mL of supernatant was removed to measure the absorbance at 480 nm. After that, 3 mL fresh PBS buffer with the corresponding pH value was added to the release medium to maintain the original volume (7 mL) so that it was unchanged. The cumulative released amount of DOX was obtained from each measurement.

2.6 Cell culture

Human HeLa cells were cultured in Roswell Park Memorial Institute (RPMI) 1640 medium supplemented with heat inactivated FBS (10%), penicillin (100 units mL^{-1}), streptomycin (100 μg mL^{-1}), amphotericin B (fungizone, 0.25 μg mL^{-1}), and sodium bicarbonate (2 mg mL^{-1}) and placed in an incubator with a fully humidified atmosphere (37 °C, 5% CO_2, and 95% room air). V79-4 Chinese hamster lung cells (ATCC no. CCL-93) were cultured by DMEM supplemented with 10% heat-inactivated FBS, penicillin (100 units mL^{-1}), streptomycin (100 μg mL^{-1}), amphotericin B (fungizone, 0.25 μg mL^{-1}), and sodium bicarbonate (3.7 mg mL^{-1}) in a humidified incubator at fully humidified atmosphere (37 °C, 5% CO_2 and 95% room air).

2.7 MTT colorimetric assay

HeLa and V79-4 cells were separately seeded in the wells of sterile 96-well flat-bottomed culture microplates and acclimated for 24 h. Then, YC-$CaCO_3$ NSs, YC-$CaCO_3$-DOX, and free DOX were added at different concentrations (from 0.78 to 200 μg mL^{-1}), and the plates were incubated for 72 h. Afterwards, freshly prepared MTT (3-(4,5-dimethylthiazol-2-yl)-2,5-diphenyl tetrazolium bromide, 20 μL, 5 mg mL^{-1}, Sigma-Aldrich Co., St. Louis, MO, USA) in filtered PBS was added to each well of the control. Subsequently, the treated cells were incubated for another 5 h. Then, the medium was centrifuged, and 150 μL of dimethyl sulfoxide (DMSO) was added to each well to completely dissolve the dark blue formazan crystals. A microplate reader was used to measure the absorbance of the solution in each well at a wavelength of 570 nm. The extent of cell proliferation was reflected by the average value of absorbance. The results are reported as the mean cell viability ± standard deviation (SD) based on the calculations of triplicate samples.

The data from the MTT colorimetric assay were analyzed by one-way analysis of variance (ANOVA) together with Fisher's least significant difference (LSD) test using Origin Pro 8 SR1 V8.0773 software (Origin Lab Corporation, MA, USA). IC50 values were obtained by fitting dose–response curves with the Hill equation.

2.8 Cellular imaging

For confocal laser scanning microscopy (CLSM) imaging, the autofluorescence of DOX was utilized to observe its loading and intracellular distribution. Lasers at 543 nm and 360 nm were used as the excitation sources, and the fluorescent images were taken by TCS NT CLSM (Leica).

3. Results and discussion

3.1. Characterizations of the as-prepared YC-$CaCO_3$ nanomaterials

Herein, the sizes of the $CaCO_3$ nanomaterials, which were biosynthesized under the mediation of the secretion derived from yeast cells, increased from nanoparticles to nanospheres with the increase in the concentrations of Ca^{2+} and CO_3^{2-} under the same experimental conditions. Transmission electron microscopy (TEM) and high-resolution TEM (HRTEM) images were used for characterization of the morphologies and sizes of the YC-$CaCO_3$ NPs. As shown in Fig. 1a, d, g and j, the biosynthesized YC-$CaCO_3$ NPs exhibited satisfactory dispersity with a relatively uniform growing size as the concentrations of Ca^{2+} and CO_3^{2-} increased (Fig. 1b, e, h and k). With concentrations of Ca^{2+} and CO_3^{2-} from 0.02 M to 0.06 M, the obtained

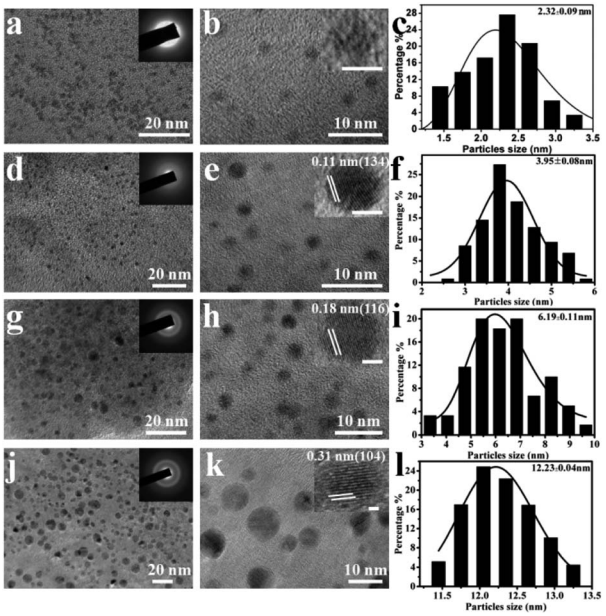

Fig. 1 (a, d, g and j) TEM and (b, e, h and k) HRTEM images and (c, f, i and l) the corresponding particle size distributions of the YC-$CaCO_3$ NPs biosynthesized in yeast cell secretions (the concentrations of Ca^{2+} and CO_3^{2-} are 0.02, 0.03, 0.05, and 0.06 M, respectively).

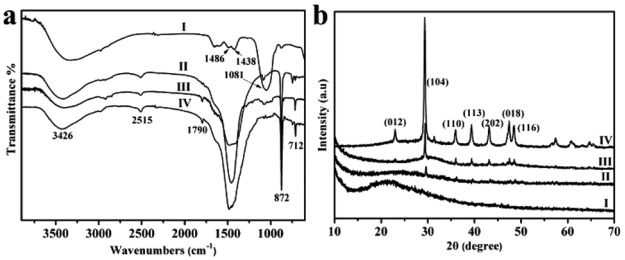

Fig. 2 FT-IR spectra (a) and XRD patterns (b) of the YC-$CaCO_3$ NPs biosynthesized in yeast cell secretions (the concentrations of Ca^{2+} and CO_3^{2-} are 0.02 (I), 0.03 (II), 0.05 (III) and 0.06 M (IV), respectively).

YC-$CaCO_3$ nanomaterials were nanoparticles (YC-$CaCO_3$ NPs) that were 2.3 nm to 12.2 nm in diameter (Fig. 1c, f, i and l).

The crystallinity of the biosynthesized YC-$CaCO_3$ NPs was determined by HRTEM. The SAED images of the obtained YC-$CaCO_3$ NPs show that the crystal types of the products were changed from amorphous to crystal with an increase in the sizes of the $CaCO_3$ nanoparticles (as shown in the insets of Fig. 1a, d, g and j). In these $CaCO_3$ crystals, the well-resolved lattice spacing distance of 0.11 nm, 0.18 nm, and 0.31 nm, respectively, corresponded to the (134), (116), and (104) crystal planes of the calcite crystalline structure of YC-$CaCO_3$ NPs, respectively, and these data were further confirmed by the following XRD characterization. Otherwise, zeta potential analysis was exploited to characterize the stability of the YC-$CaCO_3$ NPs (Fig. S2†).

The results showed that zeta potentials of these YC-$CaCO_3$ NPs with different sizes (from 2.3 nm to 12.2 nm) were −29.4 mV, −23.2 mV, −26.2 mV, and −26.3 mV, respectively, which indicate the relative stabilities of YC-$CaCO_3$ NPs in neutral PBS water.[39,40] However, when comparing the morphology with the crystals formed in distilled water, the XRD pattern of the synthesized $CaCO_3$ revealed that the samples were in the calcite phase (Fig. S3†). Thus, we can come to a definite conclusion that the secretion of yeast cells and the concentration of reactants are crucial for the formation of the YC-$CaCO_3$ NPs with different sizes.

The components of these obtained YC-$CaCO_3$ NPs were confirmed by FT-IR analyses and X-ray diffraction analysis (Fig. 2). The absorption bands of calcium carbonate in the FT-IR spectrum can be divided into four regions: $\nu_1 = 1080\ cm^{-1}$, $\nu_2 = 870\ cm^{-1}$, $\nu_3 = 1400\ cm^{-1}$ and $\nu_4 = 700\ cm^{-1}$. When the concentrations of Ca^{2+} and CO_3^{2-} are 0.02 M, it can be observed that in the FT-IR spectrum of the products, the in-plane bending of CO_3^{2-} at approximately 713 cm^{-1} (ν_4) disappears, the out-of-plane bending (ν_2) at 872 cm^{-1} and the symmetric stretch (ν_1) at 1080 cm^{-1} broaden, and the asymmetric stretch (ν_3) splits into two parts at approximately 1486 and 1438 cm^{-1}, which are consistent with the spectra of typical amorphous $CaCO_3$ (Fig. 2a(I)).[41,42]

As for the other three crystals of YC-$CaCO_3$ NPs, there are the characteristic adsorption peaks of calcite at 716 cm^{-1}, 876 cm^{-1}, 1445 cm^{-1}, and 2515 cm^{-1} (Fig. 2a(II–IV)).[43,44] In addition, the IR peaks of YC-$CaCO_3$ NPs at 3426 cm^{-1} and 1790 cm^{-1} were assigned to stretching vibrations of –OH and the typical amide absorptions of biomolecules derived from the secretion of yeast cells, respectively. Although it is still unclear how the biomolecules interact with the $CaCO_3$ NPs all through the reaction, the study using IR still provides informative indications regarding the interaction between the biomolecules and $CaCO_3$ NPs and the structural transition of the secretion of yeast used at different reaction conditions (Fig. S10 and S11†).[45]

From the above results, it can be speculated that biomolecules derived from the secretion can stabilize the unstable amorphous phase and block its transformation to the calcite phase when the concentration of yeast cell secretion is sufficiently high and if the concentrations of the reactants are constant.

The XRD result of YC-$CaCO_3$ NPs with the size of approximately 2.3 nm shows that there is a broad diffraction peak in the XRD pattern, indicating their amorphous nature (Fig. 2b(I)). Otherwise, the characteristic peaks of calcite become increasingly clear with the increase in the size of YC-$CaCO_3$ NPs (Fig. 2b(II–VI)). When the size of the YC-$CaCO_3$ NPs is approximately 12.2 nm, all reflection peaks could be well indexed to a pure rhombohedral calcite type (JCPD card no. 85-1108), and no additional peaks were observed, indicating the high purity of the as-biosynthesized $CaCO_3$ NPs. Thus, the biomolecules derived from the secretion may play a key role in the formation of these YC-$CaCO_3$ NPs, and it was supposed that a high concentration of biomolecules can inhibit the crystallization of the YC-$CaCO_3$ NPs.

Subsequently, the influences of high concentrations of reactants on the morphology and size of the products were also studied. The morphologies and sizes of $CaCO_3$ were observed by scanning electron microscopy (SEM) and TEM, and images are

shown in Fig. 3. The results indicate that the biosynthesized $CaCO_3$ changed from nanospheres (YC-$CaCO_3$ NSs) to microspheres (YC-$CaCO_3$ MSs), and the sizes of the products were 65.3 nm, 519.9 nm, 2.5 μm, and 3.6 μm, respectively, when the concentrations of reactant increased from 0.1 M to 0.4 M (Fig. 3a, d, g and h).

The TEM observations showed that the $CaCO_3$ spheres consisted of the building blocks of $CaCO_3$ nanocrystals, and then, the nanocrystals assembled together to form the hierarchical pore structures of the YC-$CaCO_3$ (Fig. 3b, e, h and k). The regions of light contrast between individual $CaCO_3$ building blocks indicate the existence of pores within the YC-$CaCO_3$. The assembly of the nanoparticles generates the porous structure to provide a three-dimensional network for these nano/microspheres. The hierarchical porous nature can increase the specific surface area and should be beneficial for the mass transmission between the interior and exterior of the materials. The results indicated that the regulating effects of the secretion on $CaCO_3$ size decreased with increasing concentrations of reactants (from 0.1 M to 0.4 M) under the mediation of the same concentration of yeast cell secretion, and the $CaCO_3$ nanoparticles can then assemble into nano/microspheres.

Here, due to the porous structure and the considerable yield, the YC-$CaCO_3$ NSs with the size of approximately 519 nm in diameter were chosen to evaluate their porous structures and behaviors as an anticancer drug carrier. For the sake of convenience, the YC-$CaCO_3$ NSs with the size of approximately 519 nm are directly called YC-$CaCO_3$ NSs in the following characterizations. A magnified FESEM image (Fig. 4a) clearly shows the porous property of the YC-$CaCO_3$ NSs, which resembles that of natural coral with a porous structure (Fig. 4b).

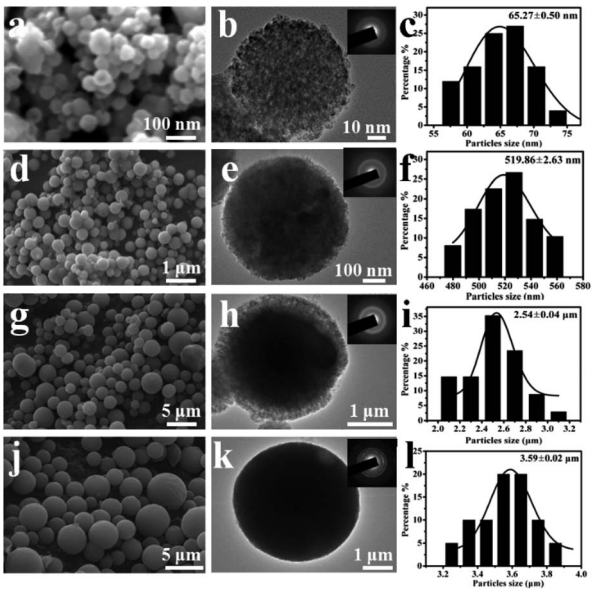

Fig. 3 SEM (a, d, g, and j) and TEM (b, e, h, and k) images and the corresponding particle size distributions (c, f, i, and l) of the YC-$CaCO_3$ nano/microspheres biosynthesized in the same concentration of yeast cell secretions (the concentrations of Ca^{2+} and CO_3^{2-} were 0.1 M (a–c), 0.2 M (d–f), 0.3 M (g–i), and 0.4 M (j–l)).

Fig. 4c shows the obvious contrast between the dark nanoparticles and pale margins, and this denotes the porous nature of the YC-$CaCO_3$ NSs.

The HRTEM of the YC-$CaCO_3$ NSs further confirmed that the regions of light contrast between the $CaCO_3$ nano building blocks indicated the presence of pores in the YC-$CaCO_3$ NSs (Fig. 4d). Further observations from the HRTEM imaging indicated the good crystalline nature of the YC-$CaCO_3$ NSs. The results showed that porous nanostructures were fabricated with high specific surface area and good adsorption capacities. The FT-IR spectrum of the YC-$CaCO_3$ NSs indicates that the product is composed of a vaterite phase, which is consistent with the above XRD results (Fig. 4e). The FT-IR results also indicated that there might be strong coordination between the YC-$CaCO_3$ NSs and the biomolecules from the yeast secretion based on the spectra of the functional groups –OH, C=O, and $–NH_2$.

Considering that biomolecules from the secretion of yeast cells play a key role in the formation of YC-$CaCO_3$ NSs, we determined how many biomolecules were involved in this process. Therefore, TG curves of the YC-$CaCO_3$ NSs were further characterized to determine the amount of the biomolecules coordinated with the products. The experiment was carried out under an air atmosphere at a heating rate of 5 deg min^{-1} from 30 °C to 900 °C (Fig. 4f). There were three obvious weight loss processes. The first change was from 30 °C to 310 °C, and the mass of the sample decreased approximately 7.52%, which was caused by the loss of water and low molecular weight biomolecules. The second change occurred from 310 °C to 610 °C, in which there was a weight loss of 6.28% that was caused by the decomposition of high molecular weight biomolecules. The last occurrence of weight loss was from 610 °C to 780 °C, and was attributed to the decomposition of $CaCO_3$. The evidence clearly shows that a certain amount of biomolecules was chelated into the YC-$CaCO_3$ NSs. From the above results, we can come to

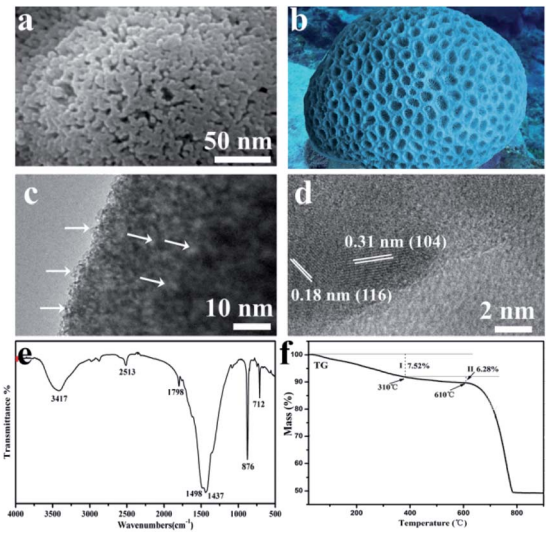

Fig. 4 (a) A typical FESEM image of the YC-$CaCO_3$ NSs, revealing their pore texture; (b) a photo of coral; (c) TEM and (d) HRTEM images of the YC-$CaCO_3$ NSs; (e) FT-IR spectrum of YC-$CaCO_3$ NSs; and (f) TGA data obtained from YC-$CaCO_3$ NSs.

a definite conclusion that the biomolecules in the yeast cell secretions are responsible for the formation of the YC-$CaCO_3$ NSs with a porous nature.

The nitrogen stripping absorption curve and pore size distributions of YC-$CaCO_3$ NSs were determined to analyze the specific surface areas and pore size, and also verify the porous structure (Fig. 5). Typical type IV isotherms with H3 type hysteresis behavior indicate the existence of mesopores with good pore connectivity inside the YC-$CaCO_3$ NSs (Fig. 5a). Furthermore, the presence of mesopores was proved from the hysteresis loop in the relatively high-pressure parts ($P/P_0 > 0.9$), and the BJH pore size distribution curve shows the wide range of pore size distributions (Fig. 5b).[46] Therefore, the abundant pore structure with efficient transport pathways would be beneficial to increase the specific surface area and the mass transport, which are important properties for catalysts, adsorption, and other applications. The Brunauer–Emmett–Teller (BET) model was adopted to calculate the specific surface areas of the YC-$CaCO_3$ NSs, and the results show that the coral-like $CaCO_3$ exhibited a specific surface area of 89.12 $m^2\ g^{-1}$ and a total pore volume of 0.80 $cm^3\ g^{-1}$. This indicates that the sample has a relatively high surface-to-volume ratio, which contributes to reducing transport lengths for mass and increases the large loading capacity.

Before the study of application performance, the formation mechanism of YC-$CaCO_3$ nanomaterials will be discussed in detail. As depicted in Fig. 6, the synthetic strategy for YC-$CaCO_3$ proceeds by two simple incubation processes involving the reactant and the secretion of the yeast cells. First, a certain amount of Ca^{2+} was added to the secretion of the yeast cells, and the mixture was maintained for 12 h under moderate stirring, in order for the Ca^{2+} to fully coordinate with the biomolecules derived from the secretion.[47,48] Second, CO_3^{2-} was added to the above solution, and a reaction between Ca^{2+} and CO_3^{2+} occurred. In the subsequent process, the amorphous $CaCO_3$ nanoparticles were first obtained in the solution under the mediation of the biomolecules from the secretion. With the development of crystallization, $CaCO_3$ nanocrystals were formed by the control of the biomolecules. When the amount of the reactants was sufficient to fabricate additional $CaCO_3$ nanocrystals, they further self-assembled into $CaCO_3$ nanospheres under the constant secretion of the yeast cells. Therefore, the biomolecules from the secretion played a key role in the construction of the $CaCO_3$ nanomaterials. Moreover, the assembly formation mechanism of nanoparticles can be

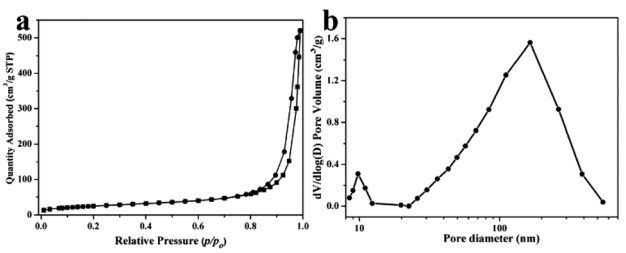

Fig. 5 (a) Nitrogen adsorption–desorption isotherms and (b) BJH desorption pore distribution curves of the YC-$CaCO_3$ NSs.

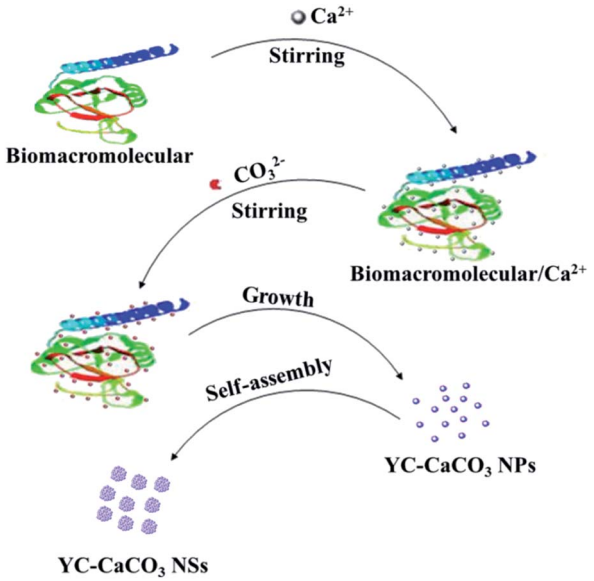

Fig. 6 Schematic illustration of the formation mechanism for the YC-$CaCO_3$ NSs.

harnessed to construct hierarchical structural nanomaterials by the regulation of soft biomolecules.

Due to the high surface area, porous structure, and satisfactory pH sensitivity, the YC-$CaCO_3$ NSs could be ideally controlled and act as sustained release anticancer drug carriers with relatively high adsorption capacity. The high specific surface area and porous structure enable the excellent adsorption capacity of the YC-$CaCO_3$ NSs. The YC-$CaCO_3$ NSs become loaded with DOX by simply incubating the nanomaterials in a DOX solution. In this situation, it is reasonably assumed that in addition to the electrostatic interaction between the negatively charged $CaCO_3$ and the positively charged DOX solution, a coordination reaction between Ca^{2+} ions and the surface oxygen groups of YC-$CaCO_3$ NSs could also result in efficient DOX loading.

The behavior of DOX as it was loaded into the YC-$CaCO_3$ NSs was studied by monitoring the loading process using UV-vis spectroscopy analysis (Fig. 7a). The concentration of DOX was determined through an established standard curve (Fig. S4†). There is a gradual equilibrium from quick adsorption to slow adsorption in the loading process of DOX. Upon careful analysis, quick adsorption occurs due to the high initial DOX concentration, which can drive DOX to enter into the porous structure of the YC-$CaCO_3$ NSs within less than 3 h. DOX then slowly enters into the relatively smaller pores of the YC-$CaCO_3$ NSs, and gradually, equilibrium can be obtained. The color change of YC-$CaCO_3$ NSs loaded with DOX (YC-$CaCO_3$-DOX) indicates the existence of a massive amount of DOX absorbed into the YC-$CaCO_3$ NSs (inset of Fig. 7a), suggesting the relatively good adsorption capacity of the YC-$CaCO_3$ NSs.

The components and the porous structure of the YC-$CaCO_3$ NSs can also bring about sustained and pH-sensitive release of DOX. For further examination, time- and pH-dependent releases of DOX were investigated (Fig. 7b). The first

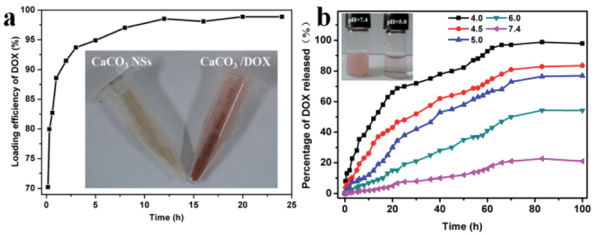

Fig. 7 (a) Loading kinetics of DOX into the YC-$CaCO_3$ NSs. The inset shows an image of the YC-$CaCO_3$ NSs (left) and YC-$CaCO_3$-DOX (right). (b) Time- and pH-dependent release of DOX from the hierarchically porous YC-$CaCO_3$ NSs at 30 °C, and the inset shows a digital image of the release systems at different pH values after 83 h.

observation is that the YC-$CaCO_3$ NSs showed well-defined pH-dependent DOX release behavior, and when the pH decreased, additional DOX release from the YC-$CaCO_3$ NSs occurred at the same time points. The drug release was relatively slow at pH 7.4, which indicated that DOX loaded into the YC-$CaCO_3$ NSs was stable at physiological pH values, and caused little toxicity to normal tissues under the neutral microenvironment. Instead, compared with the release of DOX under natural conditions, the release of DOX in a pH 4.5 buffer solution is faster due to the pH-sensitive solubility of the $CaCO_3$ component in the acidic microenvironment. These results suggest that the YC-$CaCO_3$ NSs exhibit well-defined pH-dependent drug release behavior and could controllably release additional anticancer drugs into the acid tumor microenvironment. The second observation is that the sustained release process proceeded for more than 80 h, indicating that the porous structure is beneficial for prolonging the release time of the loaded drug (Fig. 7b). All these results indicated that the $CaCO_3$ and porous structures in YC-$CaCO_3$-DOX played crucial roles in sustained and pH-sensitive release of the loaded drug. A prolonged release time of a targeted-delivery drug is desirable because it will decrease body injuries, which is favorable for cancer therapy.

The standard MTT assay was determined to evaluate the *in vitro* cytotoxicities of YC-$CaCO_3$ NSs, YC-$CaCO_3$-DOX, and DOX on V79-4 and HeLa cells (Fig. 8 and S5†). The cytotoxicities of the YC-$CaCO_3$ NSs, YC-$CaCO_3$-DOX, and free DOX were dose-dependent. The cell inhibition rates of YC-$CaCO_3$-DOX and free DOX on V79-4 and HeLa cells obviously increased with increasing concentration. In strong comparison, the IC50 values of the YC-$CaCO_3$ NSs on V79-4 cells cannot be obtained, showing that the $CaCO_3$ nanospheres have good biocompatibility (Fig. S5†). Furthermore, the IC50 value of YC-$CaCO_3$-DOX on V79-4 cells was higher than that of YC-$CaCO_3$-DOX on HeLa cells, indicating that YC-$CaCO_3$-DOX can efficiently inhibit the proliferation of cancer cells and slightly inhibit the proliferation of V79-4 normal cells. The explanation for this may primarily lie in the fact that YC-$CaCO_3$-DOX can release DOX in extracellular sites in tumor tissues (pH 5.5) or lysosomes (pH 4.5) in cancer cells, which is attributed to the excellent pH response and release of DOX in the acidic microenvironment. Further observation showed that the IC50 value of DOX on HeLa cells was lower than that of YC-$CaCO_3$-DOX, but the IC50 value of

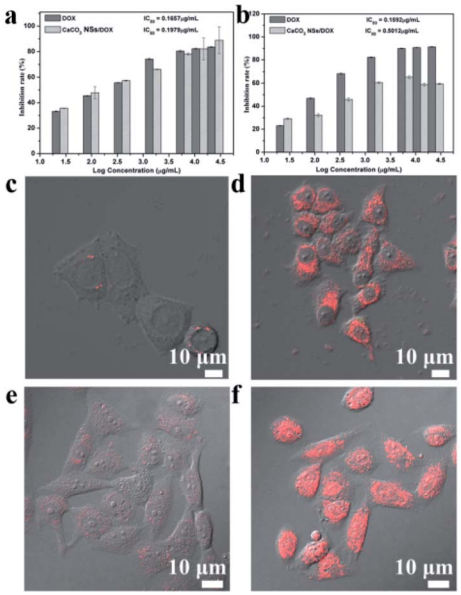

Fig. 8 *In vitro* cytotoxicities of DOX and YC-$CaCO_3$-DOX on (a) HeLa cells and (b) V79-4 normal cells after incubation for 72 h. CLSM images of (c and e) V79-4 normal cells and (d and f) HeLa cells incubated with YC-$CaCO_3$-DOX for 24 h and 72 h, respectively.

DOX on V79-4 cells was lower than that of YC-$CaCO_3$-DOX. This suggests that the toxicity of YC-$CaCO_3$-DOX to normal tissues is low, which will reduce the spread of toxic drugs to normal tissues while enhancing drug delivery efficiency and also enhancing the anticancer effect.[49]

To determine the intracellular uptake behaviors of YC-$CaCO_3$-DOX, V79-4 cells, and HeLa cells incubated with YC-$CaCO_3$-DOX for 24 h were observed by CLSM (Fig. 8c and d). It was observed that the red fluorescence of DOX was widely spread inside the HeLa cells, while there was only a small amount of red fluorescence seen in the V79 cells after 24 h incubation with YC-$CaCO_3$-DOX. Overall, the advantages and properties of this anticancer drug deliverer have the potential to selectively and effectively release a drug in the acidic tumor microenvironment. The characteristics of sustained and pH-sensitive release of a drug will decrease the dosing frequency of toxic anticancer drugs, which could reduce the damage to normal tissues and improve patient compliance.

4. Conclusions

Yeast cell-mediated calcium carbonate nanoparticles (or nanospheres) (YC-$CaCO_3$ NPs/NSs) were fabricated for the first time using a facile and green method. The biomolecules, derived from the secretion of yeast cells, can be used as conditioning and stabilizing agents to control the biosynthesis of the YC-$CaCO_3$ NPs/NSs. The morphology, size, and crystal forms of the biosynthesized YC-$CaCO_3$ nanomaterials can be tuned by the concentrations of biomolecules from the secretion of yeast cells. With an increase in the concentration of biomolecules, the morphologies and crystal forms of $CaCO_3$ changed from amorphous nanoparticles to calcite nanospheres. In addition,

the $CaCO_3$ materials synthesized in the secretion of yeast cells exhibited satisfactory biocompatibility and pH-dependent sustained drug-release performances, while the porous structure endowed them with high drug-loading capacity. This work presents the biomimetic synthesis of cell-mediated materials using a bioinspired strategy, and this cell-secretion-mediated method to synthesize functional nanomaterials can be used as a reference for other biomimetic syntheses of nanomaterials.

Conflicts of interest

There are no conflicts to declare.

Acknowledgements

This work was financially supported by the National Science Foundation of China (No. 21877027, 21771058, and 21601052); Program for Science Technology Innovation Teams in Universities of Henan Province (No. 19IRTSTHN023); China Postdoctoral Science Foundation (No. 2016M592294); and The 111 Project (No. D17007).

Notes and references

1 S. Yao, B. Jin, Z. Liu, C. Shao, R. Zhao, X. Wang and R. Tang, *Adv. Mater.*, 2017, **29**, 1605903.
2 C. Doonan, R. Ricco, K. Liang, D. Bradshaw and P. Falcaro, *Acc. Chem. Res.*, 2017, **50**, 1423–1432.
3 F. Nudelman and N. Sommerdijk, *Angew. Chem., Int. Ed.*, 2012, **51**, 6582–6596.
4 H. L. P. Tytgat, C. W. Lin, M. D. Levasseur, M. B. Tomek, C. Rutschmann, J. Mock, N. Liebscher, N. Terasaka, Y. Azuma, M. Wetter, M. F. Bachmann, D. Hilvert, M. Aebi and T. G. Keys, *Nat. Commun.*, 2019, **10**, 5403.
5 Y. J. Lee, H. Yi, W.-J. Kim, K. Kang, D. S. Yun, M. S. Strano, G. Ceder and A. M. Belcher, *Science*, 2009, **324**, 1051.
6 G. Vargas, J. Cypriano, T. Correa, P. Leao, D. A. Bazylinski and F. Abreu, *Molecules*, 2018, **23**, 2438.
7 F. Mickoleit, C. Lanzloth and D. Schuler, *Small*, 2020, **16**, 1906922.
8 Y. Shang, N. Li, S. Liu, L. Wang, Z.-G. Wang, Z. Zhang and B. Ding, *Adv. Mater.*, 2020, **32**, 2000294.
9 B. Liu, Y. Cao, Z. Huang, Y. Duan and S. Che, *Adv. Mater.*, 2015, **27**, 479–497.
10 N. Kröger, R. Deutzmann and M. Sumper, *Science*, 1999, **286**, 1129.
11 Y. Chang, T. Liu, P. Liu, L. Meng, S. Li, Y. Guo, L. Yang and X. Ma, *Chem. Commun.*, 2020, **56**, 5693–5696.
12 A. S. Ball, S. Patil and S. Soni, in *Methods in Microbiology*, ed. V. Gurtler, A. S. Ball and S. Soni, Academic Press, 2019, vol. 46, pp. 1–18.
13 W. Qin, C. Y. Wang, Y. X. Ma, M. J. Shen, J. Li, K. Jiao, F. R. Tay and L. N. Niu, *Adv. Mater.*, 2020, **32**, e1907833.
14 T. J. Park, K. G. Lee and S. Y. Lee, *Appl. Microbiol. Biotechnol.*, 2016, **100**, 521–534.
15 K. K. Sand, S. Jelavić, S. Dobberschütz, P. D. Ashby, M. J. Marshall, K. Dideriksen, S. L. S. Stipp, S. N. Kerisit, R. W. Friddle and J. J. DeYoreo, *Nanoscale Adv.*, 2020, **2**(8), 3323–3333.
16 J. Sun, C. Chen, H. Pan, Y. Chen, C. Mao, W. Wang, R. Tang and X. Gu, *J. Mater. Chem. B*, 2014, **2**, 4544–4553.
17 P. Bao, M. Xia, A. Liu, M. Wang, L. Shen, R. Yu, Y. Liu, J. Li, X. Wu, C. Fang, M. Chen, G. Qiu and W. Zeng, *RSC Adv.*, 2018, **8**, 22635–22642.
18 Y. Liu, C. Ding, L. He, X. Yang, Y. Gou, X. Xu, Y. Liu, C. Zhao, J. Li and J. Li, *J. Mater. Chem. B*, 2018, **6**, 1984–1994.
19 X. Wang, Y.-Q. Deng, D. Yang, Y. Xiao, H. Zhao, Q.-G. Nian, X. Xu, X.-F. Li, R. Tang and C.-F. Qin, *Chem. Sci.*, 2017, **8**, 8240–8246.
20 P. Du, R. Liu, S. Sun, H. Dong, R. Zhao, R. Tang, J. Dai, H. Yin, J. Luo, Z. Liu and H. Guo, *Nanoscale*, 2019, **11**, 22748–22761.
21 S. Sabbarwal, A. K. Dubey, M. Pandey and M. Kumar, *J. Mater. Chem. B*, 2020, 5729–5744.
22 H. Lu, H. Lutz, S. J. Roeters, M. A. Hood, A. Schäfer, R. Muñoz-Espí, R. Berger, M. Bonn and T. Weidner, *J. Am. Chem. Soc.*, 2018, **140**, 2793–2796.
23 C. Qi, S. Musetti, L.-H. Fu, Y.-J. Zhu and L. Huang, *Chem. Soc. Rev.*, 2019, **48**, 2698–2737.
24 V. K. Sharma, J. Filip, R. Zboril and R. S. Varma, *Chem. Soc. Rev.*, 2015, **44**, 8410–8423.
25 J. Han, K. Liu, R. Wang, Y. Zhang and B. Zhou, *Aquat. Toxicol.*, 2019, **214**, 105236.
26 H.-B. Yao, J. Ge, L.-B. Mao, Y.-X. Yan and S.-H. Yu, *Adv. Mater.*, 2014, **26**, 163–188.
27 X. Yang, D. Yang, Y. Yan, S. G. Li, Z. M. Han, Y. H. Ji, G. L. Zheng, L. P. Xie and R. Q. Zhang, *Int. J. Biol. Macromol.*, 2020, **156**, 302–313.
28 X. Ma, X. Zhang, L. Yang, G. Wang, K. Jiang, G. Wu, W. Cui and Z. Wei, *Nanoscale*, 2016, **8**, 8687–8695.
29 X. M. Ma, L. P. Li, L. Yang, C. Y. Su, K. Wang, S. B. Yuan and J. G. Zhou, *J. Hazard. Mater.*, 2012, **209**, 467–477.
30 X. Ma, S. Yuan, L. Yang, L. Li, X. Zhang, C. Su and K. Wang, *CrystEngComm*, 2013, **15**, 8288–8299.
31 X. M. Ma, H. F. Chen, L. Yang, K. Wang, Y. M. Guo and L. Yuan, *Angew. Chem., Int. Ed.*, 2011, **50**, 7414–7417.
32 X. Ma, Y. Zhu, P. Yang, Z. Wei, P. Liu, L. Yang and K. Wang, *New J. Chem.*, 2016, **40**, 6874–6880.
33 H. Du and E. Amstad, *Angew. Chem., Int. Ed.*, 2020, **59**, 1798–1816.
34 D. S. Sevilgen, A. A. Venn, M. Y. Hu, E. Tambutte, D. de Beer, V. Planas-Bielsa and S. Tambutte, *Sci. Adv.*, 2019, **5**, 9.
35 Z. Dong, L. Feng, Y. Hao, M. Chen, M. Gao, Y. Chao, H. Zhao, W. Zhu, J. Liu, C. Liang, Q. Zhang and Z. Liu, *J. Am. Chem. Soc.*, 2018, **140**, 2165–2178.
36 W. Wei, G. H. Ma, G. Hu, D. Yu, T. Mcleish, Z. G. Su and Z. Y. Shen, *J. Am. Chem. Soc.*, 2008, **130**, 15808–15810.
37 Y. Bae, S. Fukushima, A. Harada and K. Kataoka, *Angew. Chem., Int. Ed.*, 2003, **42**, 4640–4643.
38 G. Helmlinger, F. Yuan, M. Dellian and R. K. Jain, *Nat. Med.*, 1997, **3**, 177–182.
39 V. B. Patravale, A. A. Date and R. M. Kulkarni, *J. Pharm. Pharmacol.*, 2004, **56**, 827–840.
40 S. Bhattacharjee, *J. Controlled Release*, 2016, **235**, 337–351.

41 L. Addadi, S. Raz and S. Weiner, *Adv. Mater.*, 2003, **15**, 959–970.
42 F. M. Michel, J. MacDonald, J. Feng, B. L. Phillips, L. Ehm, C. Tarabrella, J. B. Parise and R. J. Reeder, *Chem. Mater.*, 2008, **20**, 4720–4728.
43 G. Falini, S. Albeck, S. Weiner and L. Addadi, *Science*, 1996, **271**, 67–69.
44 F. Z. Huang, Y. H. Shen, A. J. Xie, S. H. Yu, L. Chen, B. C. Zhang and W. G. Chang, *Cryst. Growth Des.*, 2009, **9**, 722–727.
45 D. V. Leff, L. Brandt and J. R. Heath, *Langmuir*, 1996, **12**, 4723–4730.
46 X. Lin, T. Ma and Z. Yuan, *Chem. Eng. J.*, 2011, **166**, 1144–1151.
47 L. B. Mao, H. L. Gao, H. B. Yao, L. Liu, H. Colfen, G. Liu, S. M. Chen, S. K. Li, Y. X. Yan, Y. Y. Liu and S. H. Yu, *Science*, 2016, **354**, 107–110.
48 C. Mao, A. Liu and B. Cao, *Angew. Chem., Int. Ed.*, 2009, **48**, 6790–6810.
49 Q. Zhao, Z. Mao, C. Gao and J. Shen, *J. Biomater. Sci., Polym. Ed.*, 2006, **17**, 997–1014.